Laparoscopic Camera Based on an Orthogonal Magnet Arrangement

Nicolo Garbin, *Student Member, IEEE*, Piotr R. Slawinski, *Student Member, IEEE*, Gregorio Aiello, Christina Karraz, and Pietro Valdastri, *Senior Member, IEEE*

***Abstract*—In this letter, we present for the first time a magnetic anchoring-actuation link with an auto-flip feature. This orthogonal magnetic arrangement relies on the placement of two permanent magnets such that their magnetic moments are respectfully orthogonal. Though the arrangement may have many applications, in this study we integrate it in a small factor magnetic camera for minimally invasive procedures. Upon insertion through a trocar incision, the 5.5 mm diameter and 35 mm length magnetic camera is coupled with an external robotic controller and displaced from the port thus preventing clutter of the surgical workspace. The device allows for manual lateral translation as well as robotically controlled tilt and pan, resulting in four degrees of freedom. The auto-flip feature prevents the need for image adjustment in software as the camera tilts through its hemispherical workspace. A static model that relates an input external control tilt and output camera tilt has been developed and validated. Favorable results during bench and canine cadaver evaluation suggest promise for the proposed magnetic camera to improve the state of art in minimally invasive surgical procedures.**

***Index Terms*—Minimally Invasive Surgery, Magnetic Actuation, Pediatric Surgery, Robotic, Endoscope.**

I. Introduction

MINIMALLY invasive surgery (MIS) as well as laparoendoscopic single site (LESS) surgery are well established techniques for abdominal procedures [1], [2]. Benefits of MIS and LESS include decreased trauma and risk, lower procedural cost, and expedited recovery for the patient [3]. Current research in surgical instrumentation aims to further reduce invasiveness, while continuing to improve efficacy through enhanced surgical dexterity and access [4].

Magnetic coupling enables transmission of force and torque through the abdominal surface allowing for anchoring and actuation of intracavitary devices [5], [6]. Magnetic devices do not require dedicated ports and introduce benefits such as improved triangulation and prevention of trocar crowding [7], [8]. The majority of magnetic surgical devices developed to date are imaging systems, of which, Caddedu et al. conducted successful human trials in 2009 [9]. Controlling camera orientation in a precise and smooth manner is necessary to provide the operator with a stable view of the area of interest [10]. Limitations of past work include restricted tilt range [9], [11], the use of complex and bulky electromagnetic drivers [12], or the need for on board motors [13], [14].

In this letter, we present for the first time an orthogonal magnet arrangement (OMA) that allows for the pan and tilt of a magnetically anchored device with a mechanical auto-flip that compensates for dipole-dipole singularity. This arrangement, consisting of two internal permanent magnets (IPMs) and an external permanent magnet (EPM) coupled with a motor, has been developed and evaluated as the core component of a magnetic camera for laparoscopic procedures (Fig. 1), though the concept is scalable and can be applied to address other clinical needs. The proposed magnetic camera (MC) is 5.5 mm in diameter and has 4 Degrees of Freedom (DoF): robotic actuation of pan and tilt of the camera, as well as the ability to passively reposition the device along the abdominal wall. As the camera is tilted through 180°, the mechanical auto-flip is convenient since no software for correcting the image is necessary. In the following text are described the principle of operation of the OMA, its theoretical modeling, and the results of bench-top and cadaver trials. The small form factor of the MC is ideal for laparoscopic procedures where space is constrained, such as MIS or robotic surgery in pediatric patients [15] [16].

II. Materials and Methods

A. Principle of Operation

Typically, magnetic instruments for laparoscopic surgery consist of an exterior body that embeds an EPM and an intra-abdominal device that embeds IPM(s) [5]–[9], [11], [13], [17]. Referring to Fig. 2.a, magnetic coupling provides two gross translational DoF and a rotational DoF (pan) that are enabled via manipulation of the EPM: changing X_{EPM}, Y_{EPM}, and Γ results in a corresponding variation in X_{IPMs}, Y_{IPMs}, and γ.

In addition, the magnet arrangement that we propose – the OMA – provides a tilt DoF that can be controlled in a hemispherical workspace (i.e., range 0°-180°) with no need for flipping the image as the camera crosses the $\alpha = 90°$ position. The OMA consists of a cylindrical EPM with diametrical magnetization (indicated as M1 in Fig. 2.b) and two IPMs: a spherical permanent magnet (M2 in Fig. 2.b) that functions as the center of rotation of tilt, and a cylindrical and diametrically magnetized permanent magnet (M3 in Fig. 2.b) that is placed in proximity of the first. Axial rotation of the EPM by an angle β results in a change in M1 orientation that, in turn, induces a tilt angle α of the internal device. This DoF can be achieved with the use of a single spherical IPM, though the symmetry of the magnetic field causes a singularity in the magnetic link.

Manuscript received August 31, 2015; accepted January 16, 2016. Date of publication February 11, 2016; date of current version March 4, 2016. This paper was recommended for publication by Associate Editor D. Stoyanov and Editor A. Bicchi upon evaluation of the reviewers' comments. This work was supported by the National Science Foundation (NSF) under Grant IIS-1453129 and Grant GRFP-1445197. Any opinions, findings and conclusions or recommendations expressed in this material are those of the authors and do not necessarily reflect the views of the NSF.

The authors are with the STORM Lab, Department of Mechanical Engineering, Vanderbilt University, Nashville, TN 37235 USA (e-mail: nicolo.garbin.1@vanderbilt.edu; p.valdastri@vanderbilt.edu).

Digital Object Identifier 10.1109/LRA.2016.2528303

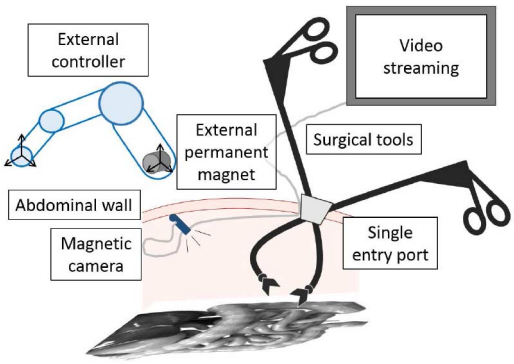

Fig. 1. The proposed magnetic camera in a LESS surgical procedure. Once deployed inside the abdominal cavity, the camera can be optimally positioned to improve triangulation for the surgeon. The wiring required for power and communication can be placed on the side of the entry port, thus not requiring a dedicated access port for the camera.

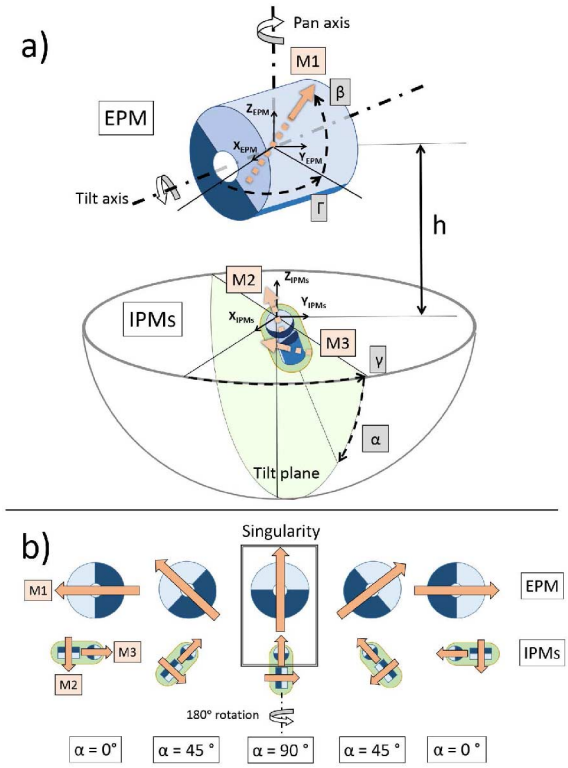

Fig. 2. (a) Schematic view of the EPM and IPMs with their reference frames. (b) Sequence along the tilt plane highlighting the auto-flip of the IPMs for $\alpha = 90°$.

This symmetry results in infinite possible orientations of the internal device along its main axis. To compensate for such singularity, the additional IPM in the OMA is positioned so that its magnetization M3 is orthogonal to M2 and thus defines a unique orientation of the device throughout the tilt range, while simultaneously generating additional attraction forces and torques used to control the device. The auto-flip feature resulting from this specific magnet arrangement allows the MC to always maintain an intuitive image orientation, thus avoiding the additional computational burden of software correction.

B. Theoretical Modeling

While the two translational DoF and the pan of magnetic surgical instruments have been introduced and modeled elsewhere

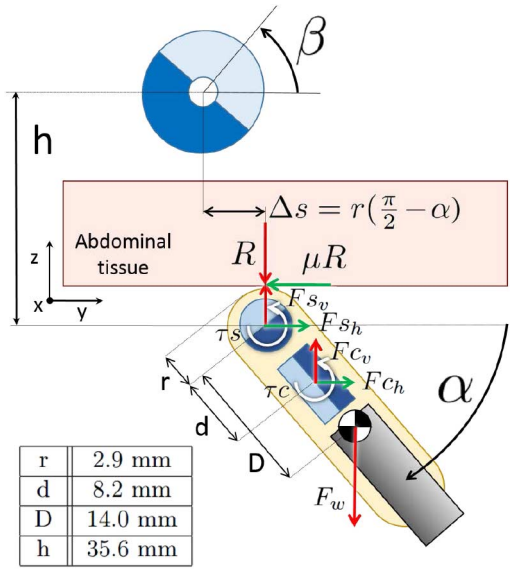

r	2.9 mm
d	8.2 mm
D	14.0 mm
h	35.6 mm

Fig. 3. Free body diagram and values of the main geometrical parameters of the magnetic camera based on the OMA.

[18], here we focus on modeling the tilting motion of the OMA as we believe this is the main innovative feature of the proposed magnet arrangement. A static force and torque model as well as finite element analysis (FEA) simulations were utilized to quantify the tilt and establish a relationship between the β tilt angle of the EPM and α tilt angle of the IPMs. These models are later experimentally validated.

A 2D free body diagram was used to develop a static model along the tilt plane represented in Fig. 2.a. Owing to low velocities, inertial terms can be neglected.

Referring to Fig. 3, the forces and torque induced by the EPM on the spherical IPM are Fs_v, Fs_h, and τs, while those induced on the cylindrical IPM are Fc_v, Fc_h, and τc. The weight force, F_w, is the only applied external force and may be generalized for any payload. The use of highly compliant and lightweight electrical wiring (see section II-C for details) allows for neglecting imposed constraint forces. Reaction force R is present owing to contact with abdominal tissue. By consequence, a friction force μR acts along the y axis. The distance between the center of mass and the center of the spherical IPM is defined as D, while the distance between centers of the two IPMs is defined as d. The axes of rotation of the EPM and spherical IPM are separated by a constant distance h along z, and Δs along y. The following equations of static equilibrium result from the applied forces:

$$\sum F_y : Fs_h(\beta,\alpha) + Fc_h(\beta,\alpha) = \mu R; \quad (1)$$

$$\sum F_z : Fs_v(\beta,\alpha) + Fc_v(\beta,\alpha) - F_w = R; \quad (2)$$

$$\sum M_x : \tau s(\beta,\alpha) + \tau c(\beta,\alpha) - F_w(\beta,\alpha)Dcos(\alpha) + Fc_v(\beta,\alpha)dcos(\alpha) + Fc_h(\beta,\alpha)dsin(\alpha) + \mu Rr = 0. \quad (3)$$

All magnetic forces and torques are dependent on both the positions (h and Δs) and tilts (α and β) of the EPM and IPMs. These were determined via FEA simulation (Comsol Multiphysics, Sweden). Forces and torques induced on each magnet were computed individually and superimposed,

following the linearity of Maxwell's magneto-static equations ($\nabla \cdot B = 0; \nabla \times B = \frac{J}{c^2 \epsilon_0}$, where J represent a steady current density, c the speed of light, and ϵ_0 the dielectric permittivity of vacuum) [19]. This assumption holds in absence of ferromagnetic materials beyond the accounted for permanent magnets. The interaction between IPMs can be neglected owing to their constrained nature. The simulations were made by varying the tilt angle α in a range of 0° to 90° with an incremental step of 9°. Owing to symmetry of the OMA, only half of the 180° tilt span needs to be modeled. Simultaneously, β was varied in the range α to α - 60° with an incremental step of 6°. By mapping forces and torques over the aforementioned span of α and β and utilizing equations 1–3, it is always possible to unequivocally determine one of the tilt angles given the other.

In order to develop a model that approximates the device behavior in a surgical scenario, tissue interaction and relative lateral displacement between EPM and IPMs must be considered. Local tissue deformation and normal force owing to magnetic attraction acting normal to the abdominal wall (Fc_v, Fs_v) suggest that the surface be better approximated as infinitely rough ($\mu = \infty$). A no-slip condition allows us to quantify, owing to assumed pure rotational motion of the OMA, a displacement of the center of rotation as $\Delta s = r(\frac{\pi}{2} - \alpha)$, where r represents the radius of the rotation.

Solely for verifying this modeling approach, an intermediate model was also developed. The ***pure-tilt*** model assumes an idealized constant point of rotation about the center of the sphere (Δs = 0), and no tissue interaction is considered (μR = 0). Equation 3 can then be simplified as follows:

$$\tau s_x(\beta,\alpha) + \tau c_x(\beta,\alpha) - F_w D cos(\alpha) + F c_v(\beta,\alpha) d cos(\alpha) + F c_h(\beta,\alpha) d sin(\alpha) = 0. \quad (4)$$

Validation of this concept with experimental data suggests that this modeling methodology is accurate and can be further developed to account for the lateral displacement of, and friction forces acting on, the device.

In order to take into account the unconstrained nature of the device, a more representative model was developed. The ***no-slip tilt*** model accounts for the infinite friction approximation where Δs is a function of α and thus has an effect on induced forces and torques. Equation 1 and 3 are combined to take friction forces into account and thus result in:

$$\tau s_x(\beta,\alpha) + \tau c_x(\beta,\alpha) - F_w D cos(\alpha) + F c_v(\beta,\alpha) d cos(\alpha) + F c_h(\beta,\alpha) d sin(\alpha) + (F s_h(\beta,\alpha) + F c_h(\beta,\alpha)) r = 0. \quad (5)$$

These models are experimentally validated in section III.

C. Design and Fabrication

An abdominal tissue thickness upon insufflation ranging from 2 cm to 4 cm was considered when selecting the magnets for the MC and the external controller. This range is representative of patients with a body mass index up to 30 kg/m^2, thus including overweight population [20].

1) Magnetic Camera: The MC was designed to be inserted through a 5 mm laparoscopy trocar incision. The vision system is a 3.9 mm diameter miniature endoscope with embedded light source and 320x240 pixels resolution (AD-3915, Shenzhen Aidevision Technology, China). The OMA IPMs consist of a 4.1 mm diameter spherical magnet (1.32T) and a 3.155 mm diameter and 6.35 mm long cylindrical magnet (1.32T) with diametrical magnetization (K&J Magnetics, Inc, PA, USA). The capsule body was 3D printed in Vero White material (Objet Pro30, Stratasys, Israel). Electrical wires with high flexibility and low weight (Calmont, California, USA) were used to power and communicate with the camera. A Pebax 00-35 (Apollo Medical Extrusion, UT, USA) catheter (6 French gauge) with a wall thickness of 0.003" was used to embed the electrical wires. Heat-shrink tubing was utilized to ensure reliable electrical connections and to secure the camera orientation once calibrated. Finally, a thin plastic coating (EcoFlex 00-50, SmoothOn, PA, USA) was adopted to waterproof the device. This coating increases MC surface friction, which also enforces the no-slip assumption. The MC prototype results 5.5 mm in diameter, 35 mm long, and weighs 2.32 g. A picture of the MC highlighting its main components is represented in Fig. 4.a.

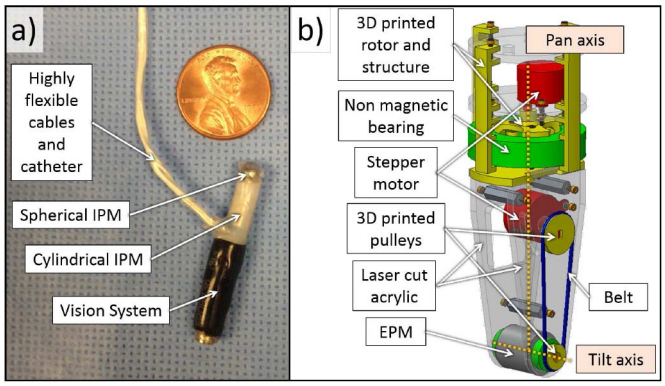

Fig. 4. (a) Magnetic camera prototype. (b) Graphic rendering of the external robotic controller.

2) External Robotic Controller: To precisely control the two rotational DoF of the EPM (25.4 mm OD, 6.35 mm ID, 25.4 mm TH, 1.32 T, also from K&J Magnetics, Inc, PA, USA), two stepper motors (28BYJ-48, Kiatronics, New Zealand) with holding torque of 15 mNm and step resolution of 0.35° were adopted. To drive the motors, stepper drivers (ULN2003, Texas Instrument, TX, USA) were controlled with a joystick embedding a dedicated microcontroller (MSP430, Texas Instrument, TX, USA). In order to avoid magnetic interference, non magnetic bearings (Igus, RI, USA) and other materials were used. The motors were placed at least 5 cm away from the EPM in order to minimize their interaction with the magnetic field. Pulley transmission was adopted to actuate the tilt angle β of the EPM. The resolution in controlling β, thus the tilt angle of the MC, can be adjusted by varying the radii of the two pulleys. The external controller, represented in Fig. 4.b, was designed to allow an easy integration with a robotic manipulator or a mechanical arm as support.

III. Validation and Results

The modeling methodology was first validated by conducting a *pure-tilt* dedicated bench-top experiment, allowing us to expand on the experiment with a more realistic no-slip assumption. The auto-flip was then characterized. The overall

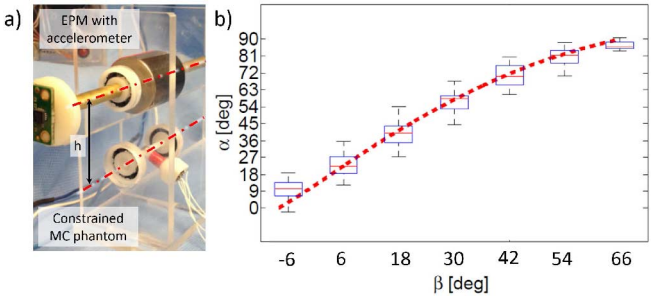

Fig. 5. (a) Experimental setup used to validate the *pure-tilt* model. (b) Experimental data in box-plot format compared with the model prediction represented as a dashed line.

device functionality was investigated via bench-top and animal cadaver trials.

A. Pure-Tilt Model Validation

To validate the *pure-tilt* model, a bench test (Fig. 5.a) was developed in which the EPM and IPMs were constrained to tilt about fixed parallel axes ($\Delta s = 0$) at a distance h of 3.56 cm. Recording EPM and IPMs angular positions via two 3-axis accelerometers (ADXL 335, Analog Device Inc., MA, USA), one placed at the EPM and one embedded with the IPMs in a MC phantom, allowed for computation of the relationship between β and α tilt angles. The accelerometers were used as inclinometers. An α range of motion from 0° to 90° was achieved by providing an input range for β from -8° to 66°. The box-plot representation of the data acquired during five different runs of this experiment are plotted in Fig. 5.b together with the model prediction resulting from equation 4.

The model can serve to predict the angle α given an input angle β with a relative error of $2\% \pm 0.95\%$. To a certain degree, the trend can be approximated as linear, though non-linearities exist in the β span of $-6°$ to 66°. The low relative error of this model shows that the previously stated assumptions (i.e., magnetic interactions between IPMs can be neglected, superposition of magnetic fields applies, and the tether does not noticeably affect MC motion) hold and can thus be utilized in the *no-slip tilt* model.

B. No-Slip Tilt Model Validation

The rolling translation of the OMA resulting from a change in α was experimentally investigated. The external robotic controller, equipped with an accelerometer as in the previous experimental setup, was placed 2 cm (h' in Fig. 6) away from an MC phantom. An acrylic sheet was used as a physical barrier. The MC phantom was equipped with a custom printed circuit board (PCB) mounting an accelerometer and a gyroscope in a single chip (LY3200ALHTR, ST Microelectronics, Switzerland) as seen in Fig. 6. The mass of the MC phantom was 2.25 g, thus very close to the MC prototype described in section II-C1.

The EPM was rotated at a constant speed of $11°/s$ through the entire workspace. Three data sets, each consisting of five consecutive full α range spans, were collected. An example of a single trial is shown in the multimedia attachment 1, while the

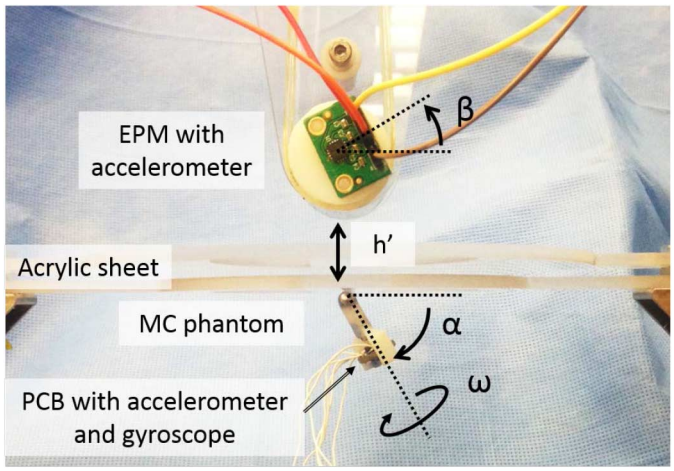

Fig. 6. Experimental setup used to validate the *no-slip tilt* model and to characterize the auto-flipping of the MC.

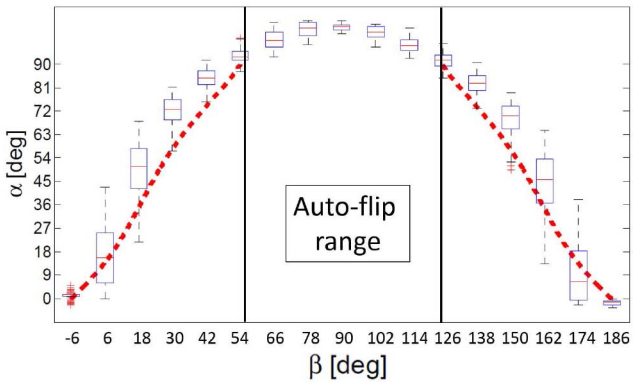

Fig. 7. Relationship between the input tilt angle β at the EPM and the MC tilt angle α from the experiments (box-plot) as compared to the theoretical model (dashed line). The region from 55° to 125° is where auto-flipping occurs.

experimental data are plotted in Fig. 7, together with the *no-slip tilt* model discussed in section II-B. From the results, we can observe that the data does not match the predicted model as well as in the pure-tilt experiment (the relative error between the average data and the model was $9.95\% \pm 4.16\%$). This may be due to imperfect orthogonality between the M2 and M3 magnetization vectors as well as a violation of the no-slip condition (slipping occurs) in the auto-flip region. Nevertheless, it is interesting to note that the relationship may be linearized in the β range of $-6°$ and 55°. As expected, workspace symmetry can be seen about $\beta = 90°$. The mid-region of the graph, the auto-flip region, corresponds to a β range between 55° to 125°.

C. Auto-Flip Characterization

The auto-flip was investigated by recording the angular velocity ω around the longitudinal axis of the MC phantom (see Fig. 6) with the same setup described in the previous section. For this trial, the EPM was rotated with an angular velocity of $52.5°/s$ so that the IPMs underwent an auto-flip, then direction was changed and this sequence repeated. The angular position β of the EPM is shown in Fig. 8 as a function of time. The MC phantom was then moving through the auto-flip region (β range between 55° to 125°). On the plot in Fig. 8 is also

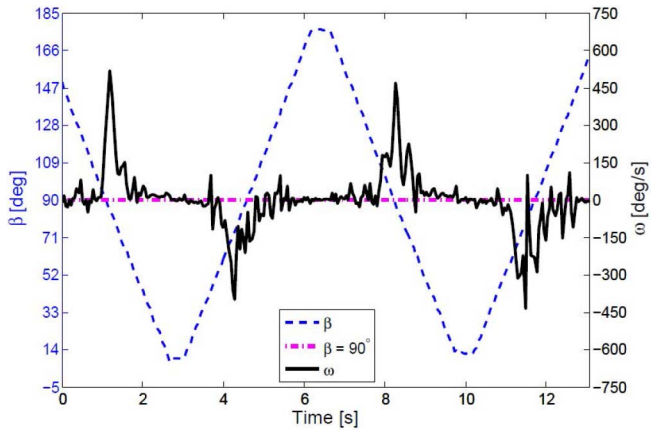

Fig. 8. Experimental characterization of the auto-flip. As the EPM tilt angle β (blue dashed line) crosses 90° (pink dashed line), auto-flipping of the MC occurs. The angular velocity ω around the longitudinal axis of the MC phantom is plotted as a black solid line.

represented the angular velocity of the MC, ω, as recorded by the gyroscope. The auto-flip is repeatable and depends on the direction of rotation of the EPM. When the EPM is rotated clockwise, the MC rotation occurs in the positive direction of the gyroscope axis, while, when the EPM is rotated counter-clockwise, ω assumes a negative value. This guarantees that the wires will not tangle if multiple auto-flips are executed. These results are further supported in Fig. 7, where the *no-slip tilt* model applies everywhere except the 55° to 125° range. Though the auto-flip is difficult to model, explicit knowledge of this range can allow for implementation of control in the linearized span, while implementing a quicker flip sequence in the auto-flip range. The auto-flip effect is clearly visible in all the three multimedia attachments.

D. MC Bench-Top Validation

The functionality of the MC prototype described in section II-C was assessed by using the external robotic controller with a pulley transmission ratio of 1 and an acrylic sheet as in Fig. 6. The motion resolution for the MC was 0.5° in tilt and 0.35° in pan (same resolution as the stepper motor). Examples of pan, tilt, and auto-flipping motions achieved during this set of experiments are available in the multimedia attachment 2. With the same setup, we also investigated the effect of increasing the intermagnetic distance h' above 2 cm. The full range of tilt motion was reliably observed for $h' \leq 41$ mm, while magnetic connection with the MC was lost for $h' > 51$ mm.

E. Cadaver Trial

The purpose of the cadaver trial was to qualitatively assess the functionality of the MC in a MIS scenario. A fresh-tissue canine cadaver (25-kg female Beagle) was utilized to mimic a small workspace as seen in pediatric patients. The surgical procedure was performed at Vanderbilt University Medical Center with the assistance and collaboration of a specially trained medical team, in accordance with all ethical considerations and the regulations related to animal experiments. Two incisions were

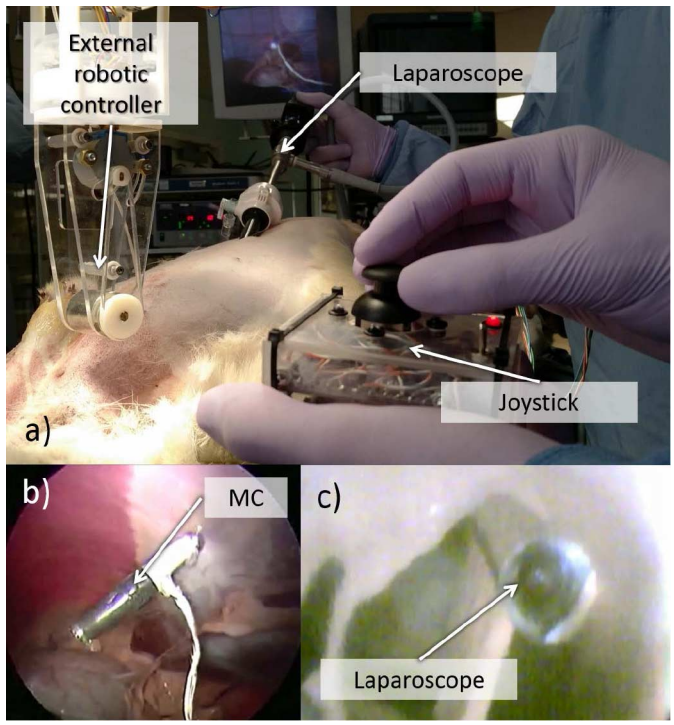

Fig. 9. (a) Photograph of the operative setup during the cadaver trial. (b) Laparoscopic view of the MC. (c) View of the laparoscope from the MC.

made in the abdomen, the first of about 15 mm, placed in the lower quadrant along the anterior axillary line, and the second of 5 mm, just inferior to the sub-costal margin, for introducing the MC. The abdominal thickness was measured at the insertion point as 1 cm. Then, a 12-mm laparoscopic port was placed in the lower incision, and a pneumoperitoneum was achieved with carbon dioxide gas.

The MC was introduced through the upper incision along with 20 cm of cable and anchored to the intra-abdominal wall using the external robotic controller placed close to the skin, as represented in Fig. 9.a. Once anchored, the camera was shifted along the abdomen and placed to focus on the liver area. We evaluated the full pan and tilt range by operating the EPM with the joystick. A standard laparoscopic camera (frame rate 30 fps, field of view 85°) introduced through the 12-mm port was used to visualize the MC while tilting and to record the image stream.

To simulate accidental magnetic decoupling, the EPM was displaced vertically to allow the MC to fall in the abdomen. Magnetic coupling was easily reengaged once the external robotic controller was brought back to its original position. A fallen camera may become dirty, though it may be cleaned via laparoscopic grasper and gauze within the cavity.

Static frames of the MC as observed by the laparoscope and of the laparoscope as visualized by the MC are represented in Fig. 9.b and Fig. 9.c, respectively. Full pan, tilt, and auto-flipping motions of the MC are included in the multimedia attachment 3. During the cadaver trials, the MC qualitatively confirmed the same range of motion and resolution observed during bench-top trials, Fig. 10. Magnetic coupling was always reliable and camera image was stable whenever the external controller was not activated. No significant image vibrations, potentially caused by laparoscope motion and by pressure

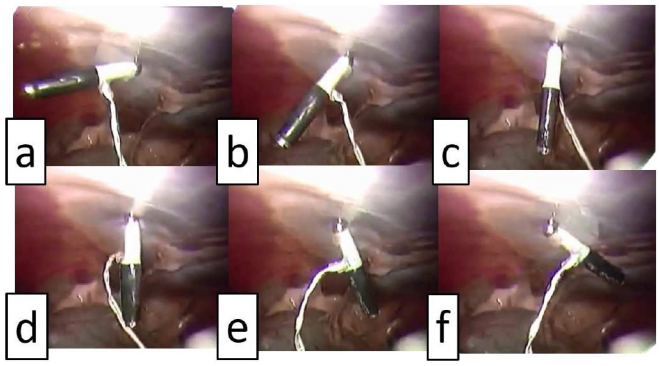

Fig. 10. Snapshots of the tilt angle control during the ex vivo trial. (a)(b): Linear and controllable range before the auto-flip regime [$-6° < \beta < 55°$]. (c)(d): auto-flip regime [$55° < \beta < 125°$]. (e)(f): Linear and controllable range after the auto-flip regime [$125° < \beta < 186°$].

regulation, were observed during operation of the MC. Image quality of the vision module integrated in the MC was below the standard for laparoscopy.

IV. Conclusion

In this work, the OMA was introduced for the first time, modeled, validated, and utilized in an MC prototype. A unique feature of the device is the auto-flip at the bottom of its hemispherical workspace that provides a controlled and repeatable rotation of the device about its own axis. An immediate use for this unique feature is to prevent the need for flipping the image as the MC crosses the vertical plane. Moving forward, a more involved modeling of the OMA behaviour will enable closed-loop control of the device both inside and outside the auto-flip region. To improve usability, sensors can be placed on the external controller to measure the magnetic moment M1 of the EPM allowing for real-time monitoring of pan and tilt of the MC, given a validated OMA model. It may benefit the user to be alerted via software of the pan and tilt angles during operation as well as whether the MC is in, or is approaching, the auto-flip region. Further usability studies will be performed once a higher resolution vision system is installed, more accurate modeling is verified, and a dedicated user interface is developed.

Although this work targets an imaging application, the OMA can be utilized in other scenarios, such as automatic suturing, where translation and rotation are both required.

The MC is a 5.5 mm by 35 mm endoscopic camera with robotic tilt and pan DoF. A "no-slip tilt" model of the device was developed to enable prediction of the OMA tilt angle given an input tilt angle of the external driving magnet. Bench top testing was conducted to confirm model validity. This model was made with an infinite contact friction assumption, however, this resulted in a large error owing to slipping of the MC in the auto-flip region. Further modeling of the deformation at the tissue surface as well as slipping of the device is necessary to achieve a smaller error that, in turn, would allow for a robust control of the device. It is worth mentioning that models that also take into account tissue deformation must be validated in a more realistic bench-top setup, where excised tissue or a tissue simulator is interposed in between the EPM and the IPMs.

Successful fresh-tissue cadaver trials were conducted on the MC using a canine model. Ease of device placement and operator viewing via joystick suggest that, if the image quality is improved, the MC has application for laparoscopic procedures where space is constrained, such as MIS in pediatric patients.

Acknowledgment

The authors would like to thank P. Williams and the staff at the Vanderbilt S. R. Light Surgical Facilities for Animal Trials for their time and assistance during the cadaver experiment.

References

[1] A. G. Harrell and B. T. Heniford, "Minimally invasive abdominal surgery: Lux et veritas past, present, and future," *Amer. J. Surg.*, vol. 190, no. 2, pp. 239–243, 2005.

[2] J. R. Romanelli and D. B. Earle, "Single-port laparoscopic surgery: An overview," *Surg. Endoscopy*, vol. 23, no. 7, pp. 1419–1427, 2009.

[3] J. E. Varela, S. E. Wilson, and N. T. Nguyen, "Laparoscopic surgery significantly reduces surgical-site infections compared with open surgery," *Surg. Endoscopy*, vol. 24, no. 2, pp. 270–276, 2009.

[4] F. Leong *et al.*, "Magnetic surgical instruments for robotic abdominal surgery," *IEEE Rev. Biomed. Eng.*, 2016, doi: 10.1109/RBME.2016.2521818, to be published.

[5] J. D. Raman, D. J. Scott, and J. A. Cadeddu, "Role of magnetic anchors during laparoendoscopic single site surgery and notes," *J. Endourol.*, vol. 23, no. 15, pp. 781–786, 2009.

[6] C. Di Natali, J. Buzzi, N. Garbin, M. Beccani, and P. Valdastri, "Closed-loop control of local magnetic actuation for robotic surgical instruments," *IEEE Trans. Robot.*, vol. 31, no. 1, pp. 143–156, Feb. 2015.

[7] M. Simi, G. Sardi, P. Valdastri, A. Menciassi, and P. Dario, "Magnetic levitation camera robot for endoscopic surgery," in *Proc. IEEE Int. Conf. Robot. Autom. (ICRA)*, 2011, pp. 5279–5284.

[8] N. Garbin, C. Di Natali, J. Buzzi, E. De Momi, and P. Valdastri, "Laparoscopic tissue retractor based on local magnetic actuation," *J. Med. Devices*, vol. 9, no. 1, p. 011005, 2015.

[9] J. Cadeddu *et al.*, "Novel magnetically guided intra-abdominal camera to facilitate laparoendoscopic single-site surgery: Initial human experience," *Surg. Endoscopy*, vol. 23, no. 8, pp. 1894–1899, 2009.

[10] P. Swain, R. Austin, K. Bally, and R. Trusty, "Development and testing of a tethered, independent camera for notes and single-site laparoscopic procedures," *Surg. Endoscopy*, vol. 24, no. 8, pp. 2013–2021, 2010.

[11] M. Simi, R. Pickens, A. Menciassi, S. D. Herrell, and P. Valdastri, "Fine tilt tuning of a laparoscopic camera by local magnetic actuation two-port nephrectomy experience on human cadavers," *Surg. Innov.*, vol. 20, no. 4, pp. 385–394, 2013.

[12] X. Liu, G. J. Mancini, and J. Tan, "Design of a unified active locomotion mechanism for a capsule-shaped laparoscopic camera system," in *Proc. IEEE Int. Conf. Robot. Autom. (ICRA)*, 2014, pp. 2449–2456.

[13] B. S. Terry, Z. C. Mills, J. Schoen, and M. E. Rentschler, "Single-port-access surgery with a novel magnet camera system," *IEEE Trans. Biomed. Eng.*, vol. 59, no. 4, pp. 1187–1193, Apr. 2012.

[14] T. Hu, P. K. Allen, N. J. Hogle, and D. L. Fowler, "Insertable surgical imaging device with pan, tilt, zoom, and lighting," *Int. J. Robot. Res.*, vol. 28, no. 10, pp. 1373–1386, 2009.

[15] T. Blinman and T. Ponsky, "Pediatric minimally invasive surgery: Laparoscopy and thoracoscopy in infants and children," *Pediatrics*, vol. 130, no. 3, pp. 539–549, 2012.

[16] N. E. Bruns, O. S. Soldes, and T. A. Ponsky, "Robotic surgery may not make the cut in pediatrics," *Front. Pediatr.*, vol. 3, no. 10, pp. 1–3, 2015.

[17] S. R. Platt, J. Hawks, and M. E. Rentschler, "Vision and task assistance using modular wireless in vivo surgical robots," *IEEE Trans. Biomed. Eng.*, vol. 56, no. 6, pp. 1700–1710, Jun. 2009.

[18] C. Di Natali, T. Ranzani, M. Simi, A. Menciassi, and P. Valdastri, "Trans-abdominal active magnetic linkage for robotic surgery: Concept definition and model assessment," in *Proc. IEEE Int. Conf. Robot. Autom. (ICRA)*, 2012, pp. 695–700.

[19] R. P. Feynman, R. B. Leighton, and M. Sands, *The Feynman Lectures in Physics, Mainly Electromagnetis and Matter*. Reading, MA, USA: Addison-Wesley, 1963.

[20] S. L. Best *et al.*, "Maximizing coupling strength of magnetically anchored surgical instruments: How thick can we go?" *Surg. Endoscopy*, vol. 25, no. 1, pp. 153–159, 2011.